INTERNATIONAL JOURNAL FOR NUMERICAL METHODS IN FLUIDS
Int. J. Numer. Meth. Fluids **28**: 1241–1261 (1998)

A BORE-CAPTURING FINITE VOLUME METHOD FOR OPEN-CHANNEL FLOWS

K. HU[a,*,1], C.G. MINGHAM[b,2] AND D.M. CAUSON[b,3]

[a] *Posford Duvivier, Bretton Centre, Peterborough PE3 8DW, UK*
[b] *Centre for Mathematical Modelling and Flow Analysis, The Manchester Metropolitan University, Chester Street, Manchester M1 5GD, UK*

SUMMARY

A high-resolution finite volume hydrodynamic solver is presented for open-channel flows based on the 2D shallow water equations. This Godunov-type upwind scheme uses an efficient Harten–Lax–van Leer (HLL) approximate Riemann solver capable of capturing bore waves and simulating supercritical flows. Second-order accuracy is achieved by means of MUSCL reconstruction in conjunction with a Hancock two-stage scheme for the time integration. By using a finite volume approach, the computational grid can be irregular which allows for easy boundary fitting. The method can be applied directly to model 1D flows in an open channel with a rectangular cross-section without the need to modify the scheme. Such a modification is normally required for solving the 1D St Venant equations to take account of the variation of channel width. The numerical scheme and results of three test problems are presented in this paper. © 1998 John Wiley & Sons, Ltd.

KEY WORDS: shallow water equations; finite volume; open channel; hydraulic jump

1. INTRODUCTION

Open-channel flows can be simulated by solving the 1D St Venant equations or 2D shallow water equations. Computational models of river flows based on the St Venant equations and shallow water equations are well-established tools in engineering practice [1].

Many explicit and implicit finite difference methods have been developed to solve these equations. Currently, implicit schemes are more popular than explicit schemes due to their computational efficiency. These include the Preissman scheme for the St Venant equations and the Leendertse-type method for the shallow water equations. However, these schemes do not perform well in the presence of flow discontinuities. Theoretically they are only capable of modelling subcritical flows. In river modelling, supercritical flows and hydraulic jumps often occur, particularly in the case of high flood flows. At present in such situations, either empirical formulae are used at the part of the river where supercritical flows appear, or large amounts of artificial viscosity are imposed to damp the resulting numerical oscillations. The inclusion of non-physical artificial viscosity significantly reduces the accuracy of the solution in areas with high velocity gradients. In some cases, even very high artificial viscosity cannot

* Correspondence to: Posford Duvivier, Bretton Centre, Peterborough PE3 8DW, UK.
[1] E-mail: khu@posford.co.uk
[2] E-mail: c.mingham@mmu.ac.uk
[3] E-mail: d.m.causon@mmu.ac.uk

CCC 0271–2091/98/181241–21$17.50

Received September 1997
Revised November 1997

stabilise the model. As much of the numerical stability theory is based on linear equations, implicit schemes, which are believed to be 'unconditionally' stable, may become unstable in transcritical flow conditions.

For shock wave problems, which are the aerodynamic equivalent of a 'bore' in free surface hydraulics, computational fluid dynamics (CFD) has made enormous progress. Lax and Wendroff [2] stressed the importance of models based on the conservation laws, and this gave rise to the popularity of central difference schemes such as those of Lax and Wendroff and MacCormack in the 1970s. The role of the monotonicity property, identified by Godunov [3], has recently been reconsidered and its importance has been realised, particularly since the late 1970s. For non-linear equations, Harten [4] introduced the more general framework of total variation diminishing (TVD) schemes. A series of papers by van Leer (1973–1979) led to various second-order Godunov schemes. A Godunov scheme requires a Riemann solver to solve local *Riemann problem* at cell interfaces (see Section 3.1 for details). Many approximate Riemann solvers have been developed [4–6] which are more efficient than the exact Riemann solver originally proposed by Godunov.

Following such progress in aerospace CFD, these methods have been gradually introduced into hydraulics. For a dam break problem, a classical test for supercritical flows and discontinuities, the Lax–Wendroff and MacCormack methods were used by Rajar [7], Garcia [8], Fennema and Chaudhry [9], and Alcrudo *et al.* [10]. Glaister [11] derived a Roe-type approximate Riemann solver for the St Venant equations and successfully introduced Godunov-type methods to solve the dam break problem. Toro [12] gave a modified HLL-type (Harten–Lax–van Leer) approximate solver for the shallow water equations and solved a two-dimensional dam break problem. Yang and Hsu [13] adopted the *flux vector splitting* method to obtain an approximate solution for the Riemann problem. These Godunov-type methods have produced very good results for dam break problems.

As a Godunov-type scheme requires the evaluation of the numerical fluxes at cell interfaces, a finite volume method seems to be particularly and naturally appropriate for its implementation. Unlike the equation transformation method [14] in which errors may be inevitably introduced by the approximation of the Jacobian matrix at each time step, the finite volume approach is more accurate and efficient. Alcrudo and Garcia-Navarro [15] reported a Godunov-type upwind method implemented in finite volume form using an irregular grid for hydraulic flows and the results were encouraging.

The new finite volume solver described in this paper solves the full shallow water equations. Using a term-by-term splitting technique, the shallow water equations are split into inviscid terms and source terms, including viscous terms. A Godunov-type upwind scheme is used for the convective inviscid terms where most of the numerical problems arise. Second-order accuracy is achieved by using MUSCL reconstruction in conjunction with a Hancock two-stage scheme for the time integration. An efficient HLL-type approximate Riemann solver has been used instead of the more expensive exact Riemann solver. The TVD property of the scheme is ensured by applying a pre-processing slope limiter, as part of the MUSCL reconstruction process, by which cell interface data is reconstructed from cell centre data. Green's theorem is used to evaluate the source terms.

One-dimensional flow modelling based on solving the St Venant equations is still popular in engineering practice because of its simplicity and computational efficiency. The 1D St Venant equations and 2D shallow water equations are different in respect of their conservative variables, though their derivations are similar. As a result of its flexibility with regard to grid topology, the new model based on solving the shallow water equations can be used directly for 1D modelling for a width-varied channel with rectangular cross-sections. More details are given in test problems 3 and 4 in Section 5.3.

2. GOVERNING EQUATIONS

Simplification of the Reynolds equations by depth-averaging leads to the shallow water equations. The equations are, in conservative differential form

$$\frac{\partial \zeta}{\partial t}+\frac{\partial uD}{\partial x}+\frac{\partial vD}{\partial y}=0, \tag{1}$$

$$\frac{\partial uD}{\partial t}+\frac{\partial \beta u^2 D}{\partial x}+\frac{\partial \beta uvD}{\partial y}-fvD+gD\frac{\partial \zeta}{\partial x}+\frac{\tau_{bx}}{\rho}-\frac{\tau_{wx}}{\rho}-\frac{1}{\rho}\left(\frac{\partial D\tau_{xx}}{\partial x}+\frac{\partial D\tau_{xx}}{\partial y}\right)=0, \tag{2}$$

$$\frac{\partial vD}{\partial t}+\frac{\partial \beta uvD}{\partial x}+\frac{\partial \beta v^2 D}{\partial y}+fuD+gD\frac{\partial \zeta}{\partial y}+\frac{\tau_{bx}}{\rho}-\frac{\tau_{wy}}{\rho}-\frac{1}{\rho}\left(\frac{\partial D\tau_{xy}}{\partial x}+\frac{\partial D\tau_{yy}}{\partial y}\right)=0, \tag{3}$$

where u, v are the depth-averaged velocity components in the horizontal x- and y-directions. ζ is the water surface elevation above the datum and D is the depth of water. β is a momentum correction factor due to vertical non-uniformity of the velocity distribution, f is the Coriolis force, τ_{bx} and τ_{by} are the bed friction shear stresses in the x- and y-directions respectively, τ_{wx} and τ_{wy} are the surface wind shear stresses, τ_{xx}, τ_{xy} τ_{yx} and τ_{yy} are the 'depth-averaged' shear stresses [16].

As a prelude to deriving the finite volume method, Equations (1)–(3) are re-written in integral form as a direct expression of the fundamental laws of conservation of mass, momentum and energy:

$$\frac{\partial}{\partial \boldsymbol{t}}\int_\Omega \boldsymbol{U}\,\mathrm{d}\Omega+\int_S \boldsymbol{H}\cdot\mathrm{d}\boldsymbol{S}=\int_S \boldsymbol{Q}_S\cdot\mathrm{d}\boldsymbol{S}+\int_\Omega \boldsymbol{Q}_V\,\mathrm{d}\Omega, \tag{4}$$

where

$$\boldsymbol{U}=\begin{pmatrix}\phi\\ \phi u\\ \phi v\end{pmatrix},\qquad \boldsymbol{H}\cdot\boldsymbol{S}=\begin{pmatrix}\phi(\boldsymbol{q}\cdot\boldsymbol{S})\\ \phi u(\boldsymbol{q}\cdot\boldsymbol{S})+\frac{1}{2}\beta\phi^2 S_x\\ \phi v(\boldsymbol{q}\cdot\boldsymbol{S})+\frac{1}{2}\beta\phi^2 S_y\end{pmatrix},\qquad \begin{matrix}\phi=gD\\ \boldsymbol{q}\cdot\boldsymbol{S}=\beta(uS_x+vS_y)\end{matrix}, \tag{5}$$

$$\boldsymbol{Q}_S\cdot\boldsymbol{S}=\begin{pmatrix}\left(1-\frac{1}{\beta}\right)\phi(\boldsymbol{q}\cdot\boldsymbol{S})\\ \phi g(hS_x)+\frac{1}{\rho}(\phi\tau_{xx})S_x+\frac{1}{\rho}(\phi\tau_{xy})S_y+\left(\frac{1}{2}-\frac{1}{2\beta}\right)\beta\phi^2 S_x\\ \phi g(hS_y)+\frac{1}{\rho}(\phi\tau_{xy})S_x+\frac{1}{\rho}(\phi\tau_{yy})S_y+\left(\frac{1}{2}-\frac{1}{2\beta}\right)\beta\phi^2 S_y\end{pmatrix}, \tag{6}$$

$$\boldsymbol{Q}_V = \begin{pmatrix} 0 \\ fv\phi + \dfrac{g}{\rho}(\tau_{wx} - \tau_{bx}) \\ -fu\phi + \dfrac{g}{\rho}(\tau_{wy} - \tau_{by}) \end{pmatrix}, \tag{7}$$

where Ω is an arbitrary 2D region with boundary S, (S_x, S_y) is a surface normal vector, and $\boldsymbol{H}$ is the flux tensor for inviscid flows. The source terms are contained within the vector $\boldsymbol{Q}_S$ representing viscous and bed slope terms, and the vector $\boldsymbol{Q}_V$ containing other source terms such as Coriolis force, bed and surface stresses and h is the bed height above a horizontal datum.

The Jacobians of the fluxes are

$$\boldsymbol{A} = \frac{\partial(\boldsymbol{H}\cdot\boldsymbol{S})}{\partial \boldsymbol{U}} = \begin{pmatrix} 0 & \beta S_x & \beta S_y \\ (-u(\boldsymbol{q}\cdot\boldsymbol{S}) + \beta c^2 S_x) & (\beta u S_x + \boldsymbol{q}\cdot\boldsymbol{S}) & \beta u S_y \\ (-v(\boldsymbol{q}\cdot\boldsymbol{S}) + \beta c^2 S_y) & \beta v S_x & (\beta v S_y + \boldsymbol{q}\cdot\boldsymbol{S}) \end{pmatrix}. \tag{8}$$

The respective eigenvalues $\boldsymbol{a}$ and associated eigenvectors $\boldsymbol{e}$ of the matrix $\boldsymbol{A}$ are

$$\boldsymbol{a}^1 = \boldsymbol{q}\cdot\boldsymbol{S} + \beta c|\boldsymbol{S}|, \qquad \boldsymbol{a}^2 = \boldsymbol{q}\cdot\boldsymbol{S}, \qquad \boldsymbol{a}^3 = \boldsymbol{q}\cdot\boldsymbol{S} - \beta c|\boldsymbol{S}|, \tag{9}$$

where $|\boldsymbol{S}| = (S_x^2 + S_y^2)^{1/2}$; $c = \sqrt{\phi}$ is the surface wave speed.

$$\boldsymbol{e}^1 = \begin{pmatrix} 1 \\ u + cn_x \\ v + cn_y \end{pmatrix}, \qquad \boldsymbol{e}^2 = \begin{pmatrix} 0 \\ -cn_y \\ cn_x \end{pmatrix}, \qquad \boldsymbol{e}^3 = \begin{pmatrix} 1 \\ u - cn_x \\ v - cn_y \end{pmatrix}, \qquad \begin{matrix} n_x = \dfrac{S_x}{|\boldsymbol{S}|} \\ n_y = \dfrac{S_y}{|\boldsymbol{S}|} \end{matrix}, \tag{10}$$

and (n_x, n_y) is a unit surface normal vector.

3. NUMERICAL SCHEME

The shallow water equations include convective, diffusive, gravity force, bed and surface stress terms and Coriolis force terms. From the numerical viewpoint, most of the problems arise from the non-linear convective terms. Using term-by-term operator splitting [17], the shallow water equations can be decomposed into two split equations:

$$\frac{\partial}{\partial t}\int_\Omega \boldsymbol{U}\,\mathrm{d}\Omega + \int_\Omega \boldsymbol{H}\cdot\mathrm{d}\boldsymbol{S} = 0, \tag{11}$$

$$\frac{\partial}{\partial t}\int_\Omega \boldsymbol{U}\,\mathrm{d}\Omega = \int_S \boldsymbol{Q}_S\cdot\mathrm{d}\boldsymbol{S} + \int_\Omega \boldsymbol{Q}_V\,\mathrm{d}\Omega. \tag{12}$$

A high resolution Godunov-type numerical scheme is applied to Equation (11) which models inviscid flow. Green's theorem is used to calculate the viscous terms and other source terms in Equation (12).

3.1. Inviscid terms

Equation (11) can be discretised as

$$\frac{\partial}{\partial t} \boldsymbol{U}_{i,j} \Omega_{i,j} + \sum_{m=1}^{M} \boldsymbol{H}_m \cdot \boldsymbol{S}_m = 0, \tag{13}$$

where Ω_{ij} denotes the cell volume, $\boldsymbol{S}_m$ is the *surface normal vector* of cell face m and M is the maximum number of cell faces; $\boldsymbol{H}_m$ represents the *numerical flux tensor* through cell interface m, $\boldsymbol{U}_{ij}$ is the integral average value of the flow solution vector $\boldsymbol{U}$ over cell ij.

The numerical method we propose is a Godunov-type upwind scheme. Godunov [3] showed how to make use of characteristic information within the framework of a conservative method. He proposed that the numerical flux could be obtained by solving a local Riemann problem at each cell interface. In one dimension, the Godunov scheme can be expressed as

$$\boldsymbol{U}_i^{n+1} = \boldsymbol{U}_i^n - \frac{\Delta t}{\Delta x} [\boldsymbol{F}(\boldsymbol{U}^{\mathrm{L}}_{i+1/2}, \boldsymbol{U}^{\mathrm{R}}_{i+1/2})_{x/t=0} - \boldsymbol{F}(\boldsymbol{U}^{\mathrm{L}}_{i-1/2}, \boldsymbol{U}^{\mathrm{R}}_{i-1/2})_{x/t=0}], \tag{14}$$

where $\boldsymbol{F}$ represents the numerical flux at the cell interface and $\boldsymbol{U}^{\mathrm{R}}$ and $\boldsymbol{U}^{\mathrm{L}}$ are the states on each side of the interface.

The Riemann problem can be solved exactly. The solution can be illustrated in the x–t plane shown in Figure 1. In one dimension, there are two waves: one travels to the left and the other to the right. They can either be *shock* (*bore*) or *rarefaction* (*depression*) waves. The two waves separate three constant states, namely $\boldsymbol{U}^{\mathrm{L}}$, $\boldsymbol{U}^{\mathrm{R}}$ and a new constant state $\boldsymbol{U}^*$ in the region between the left and right waves which is called the *star region* (Figure 1). The state $\boldsymbol{U}$ through a rarefaction wave varies continuously with x, whereas it jumps discontinuously through a shock wave. For two and three dimensions, there is an additional wave called a *contact wave*. In the HLL approximation, it is assumed that any differences in the parallel components are assumed to take place across the contact surface. Although this assumption is not always physically correct, numerical experiments have shown that it gives satisfactory results.

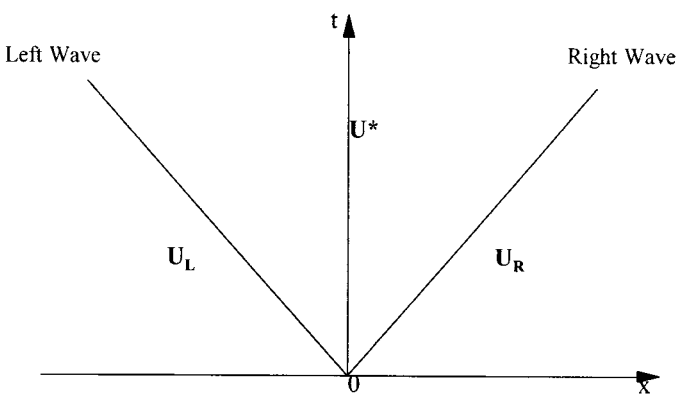

Figure 1. Wave pattern of solution of the Riemann problem.

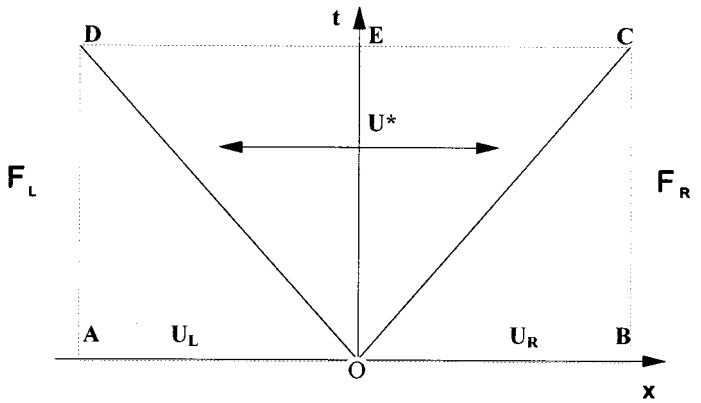

Figure 2. Sketch of HLL solution of the Riemann problem.

Since the local Riemann problem can be solved exactly, the Godunov method is fully conservative. Toro [12] gave an iterative exact Riemann solver for the reduced form of the shallow water equations.

Although in theory the Riemann problem can be solved exactly, in practice doing so is expensive, particularly for non-linear systems. Since the exact solution is averaged over the cell, we can also consider approximate Riemann solutions which require less computational work and retain the same level of accuracy. Many interesting approximate Riemann solvers have been developed [4–6]. Harten *et al.* [4] suggested an approximate solution method for Riemann problems, known as the HLL approximate Riemann solver, which we have found to be robust in application and simple to implement. Hence, we simplify and rewrite Equation (11) in one dimension:

$$\int [\boldsymbol{U}\,\mathrm{d}x - \boldsymbol{F}(\boldsymbol{U})\,\mathrm{d}t] = 0, \tag{15}$$

where $\boldsymbol{F}(\boldsymbol{U})$ represents $\boldsymbol{H}$ in one dimension.Evaluation of Equation (15) round the control volume ABCD shown in Figure 2 gives

$$|\mathrm{AO}|\boldsymbol{U}_\mathrm{L} + |\mathrm{OB}|\boldsymbol{U}_\mathrm{R} - |\mathrm{CD}|\boldsymbol{U}^* - |\mathrm{BC}|\boldsymbol{F}_\mathrm{R} + |\mathrm{DA}|\boldsymbol{F}_\mathrm{L} = 0. \tag{16}$$

If we can estimate the two wave speeds s_R and s_L, $\boldsymbol{U}^*$ can be derived as

$$\boldsymbol{U}^* = \frac{s_\mathrm{R}\boldsymbol{U}_\mathrm{R} - s_\mathrm{L}\boldsymbol{U}_\mathrm{L} - (\boldsymbol{F}_\mathrm{R} - \boldsymbol{F}_\mathrm{L})}{s_\mathrm{R} - s_\mathrm{L}}. \tag{17}$$

Similarly, integrating Equation (15) around the control volumes AOED and OBCE leads to the equations

$$\boldsymbol{U}^* = \boldsymbol{U}_\mathrm{L} + \frac{\boldsymbol{F}^* - \boldsymbol{F}_\mathrm{L}}{s_\mathrm{L}}, \tag{18}$$

$$\boldsymbol{U}^* = \boldsymbol{U}_\mathrm{R} - \frac{\boldsymbol{F}_\mathrm{R} - \boldsymbol{F}^*}{s_\mathrm{R}}. \tag{19}$$

Elimination of $\boldsymbol{U}^*$ from Equations (18) and (19) gives

$$\boldsymbol{F}^* = \frac{s_R \boldsymbol{F}_L - s_L \boldsymbol{F}_R + s_L s_R (\boldsymbol{U}_R - \boldsymbol{U}_L)}{s_R - s_L}. \tag{20}$$

In principle the numerical flux $\boldsymbol{F}^*$ could be obtained directly from $\boldsymbol{U}^*$, namely via $\boldsymbol{F}(\boldsymbol{U}^*)$. However numerical experiments have shown that Equation (20) gives excellent results in comparison with some spurious oscillations produced by using $\boldsymbol{F}(\boldsymbol{U}^*)$.

Toro [12] suggested the use of a two rarefaction wave approximation which requires the evaluation of the eigenvalues of the Jacobian matrix $\boldsymbol{A} = \partial(\boldsymbol{H} \cdot \boldsymbol{S})/\partial \boldsymbol{U}$. The wave speed estimates are

$$\begin{aligned} s_L &= \min\{q_L \cdot S - \beta c_L |S|, q^*_{TR} \cdot S - \beta c^*_{TR} |S|\}, \\ s_R &= \max\{q_R \cdot S - \beta c_R |S|, q^*_{TR} \cdot S + \beta c^*_{TR} |S|\}, \end{aligned} \tag{21}$$

where

$$\boldsymbol{q}^*_{TR} \cdot \boldsymbol{S} = \frac{1}{2}(\boldsymbol{q}_L \cdot \boldsymbol{S} + \boldsymbol{q}_R \cdot \boldsymbol{S}) + (\sqrt{\phi_L} - \sqrt{\phi_R})|\boldsymbol{S}|, \tag{22}$$

and

$$c^*_{TR} = \sqrt{\phi^*_{TR}} = \frac{1}{2}(\sqrt{\phi_L} + \sqrt{\phi_R}) - \frac{1}{4}\frac{(\boldsymbol{q}_R \cdot \boldsymbol{S} - \boldsymbol{q}_L \cdot \boldsymbol{S})}{|\boldsymbol{S}|}. \tag{23}$$

The original first-order Godunov method used a piecewise constant approximation to reconstruct the solution at cell interfaces, i.e. $\boldsymbol{U}^L$ and $\boldsymbol{U}^R$. In a MUSCL scheme, the piecewise constant approximation is replaced by piecewise linear approximation, which gives second-order spatial accuracy:

$$\hat{\boldsymbol{U}}^R_{i+1/2,\,j} = \boldsymbol{U}_{i+1,\,j} - \frac{1}{2}\Psi(r_{i+1,\,j}) \cdot \delta \boldsymbol{U}_{i+1/2,\,j}, \tag{24}$$

$$\hat{\boldsymbol{U}}^L_{i+1/2,\,j} = \boldsymbol{U}_{i,\,j} + \frac{1}{2}\Psi(r_{i,\,j}) \cdot \delta \boldsymbol{U}_{i+1/2,\,j}, \tag{25}$$

where $\delta \boldsymbol{U}_{i+1/2,\,j} = \boldsymbol{U}_{i+1,\,j} - \boldsymbol{U}_{i,\,j}$, $\delta \boldsymbol{U}_{i-1/2,\,j} = \boldsymbol{U}_{i,\,j} - \boldsymbol{U}_{i-1,\,j}$, $\boldsymbol{r}_{i,\,j} = \delta \boldsymbol{U}_{i+1/2,\,j}/\delta \boldsymbol{U}_{i-1/2,\,j}$ $\boldsymbol{r}_{i+1,\,j} = \delta \boldsymbol{U}_{i+3/2,\,j}/\delta \boldsymbol{U}_{i+1/2.\,j}$. Ψ is a *limiter* function. $\boldsymbol{r}$ is the ratio of successive gradients. The purpose of the limiter function Ψ is to limit the slope of the linear variations in order to avoid non-physical overshoots or undershoots in the numerical solution (see Figure 3). The process of interpolating cell interface values from cell centre data is known as *reconstruction*. Equations (24) and (25) show the reconstruction process in the i-direction. The reconstruction process in the j-direction can be expressed in a very similar form (omitted).

Various limiter functions can be found in the literature, e.g. the 'minmod', 'superbee' and 'van-Leer' TVD limiter functions are well-known and widely used in modern upwind schemes. Usually the 'superbee' limiter gives an excessively steep profile whilst the 'minmod' limiter produces a relatively smeared profile. It was found that the 'van-Leer' limiter, which falls in between, generally gives the best results [18].

(i) Minmod limiter: $\Psi = \max[0, \min(r, 1)]$
(ii) 'Super-bee' limiter: $\Psi = \max[0, \min(2r, 1), \min(r, 2)]$
(iii) van Leer limiter: $\Psi = (r + |r|)/(1 + r)$

To maintain stability and obtain second-order accuracy in time, a Hancock two-stage time integration method is applied [19]:

Step 1 (predictor):

$$\boldsymbol{U}_{i,j}^{p} = \boldsymbol{U}_{i,j}^{n} - \frac{1}{2}\frac{\Delta t}{\Omega_{i,j}} \sum_{m=1}^{M} \boldsymbol{H}(\boldsymbol{U}_m) \cdot \boldsymbol{S}_m. \tag{26}$$

Step 2 (corrector):

$$\boldsymbol{U}_{i,j}^{n+1} = \boldsymbol{U}_{i,j}^{p} - \frac{\Delta t}{\Omega_{i,j}} \sum_{m=1}^{M} \boldsymbol{H}(\hat{\boldsymbol{U}}^{p\mathrm{L}}, \hat{\boldsymbol{U}}^{p\mathrm{R}}) \cdot \boldsymbol{S}_m, \tag{27}$$

where $\hat{\boldsymbol{U}}^{p\mathrm{L}}$ and $\hat{\boldsymbol{U}}^{p\mathrm{R}}$ are the two states on either side of the cell interface m at time level p defining a Riemann problem.

The predictor step advances the solution to the half time level and the corrector step then computes fluxes at the half time level which are used to advance the solution to the full time step. It should be noted that the MUSCL reconstruction in step 2 of the Hancock scheme is based on the gradients of $\boldsymbol{U}^n$ not $\boldsymbol{U}^p$. Numerical experiments show that the use of data $\boldsymbol{U}^n$ gives better results than $\boldsymbol{U}^p$.

The implementation of the finite volume method via Equations (26) and (27) on arbitrary grids is simpler than either the finite element or finite difference methods because no explicit co-ordinate transformation is needed. Cell volumes and cell face side vectors, easily computed by simple vector operations, represent the transformation Jacobian and metric derivative terms; therefore the possibility of geometrically-induced errors caused by numerically discretising these terms is avoided. Additionally, since the method is unsplit, no geometrically induced errors can arise due to the approximate factorisation implicit in a split algorithm.

The method does not involve any explicitly introduced artificial viscocity terms with free parameters requiring calibration. It can thus be applied as described to a wide variety of flows involving standing bores and bore wave propagation.

3.2. Source terms

The split Equation (12) for the viscous terms, incorporating the remaining source terms, can be solved by evaluating the fluxes around cell interfaces using Green's theorem. To construct the viscous numerical fluxes, it is necessary to evaluate first-order derivatives of the velocities at each cell interface. This is not a trivial task particularly if the mesh is distorted. By the method of Jacobian transformation, Deiwert [20] provided the following approximations for the first-order derivatives:

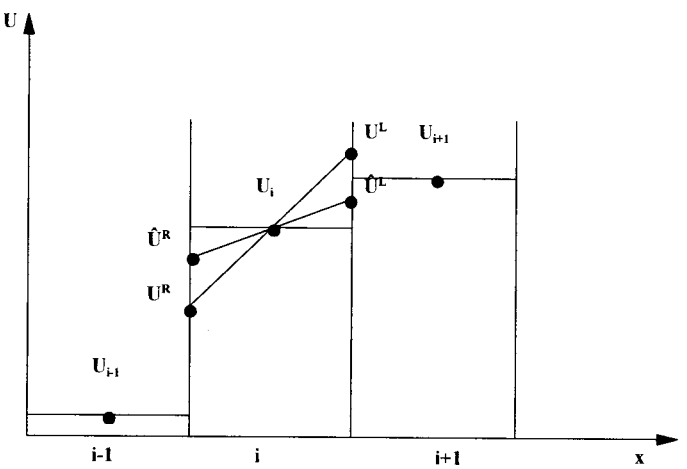

Figure 3. Overshoot from second-order interpolation and effect of the limiter function.

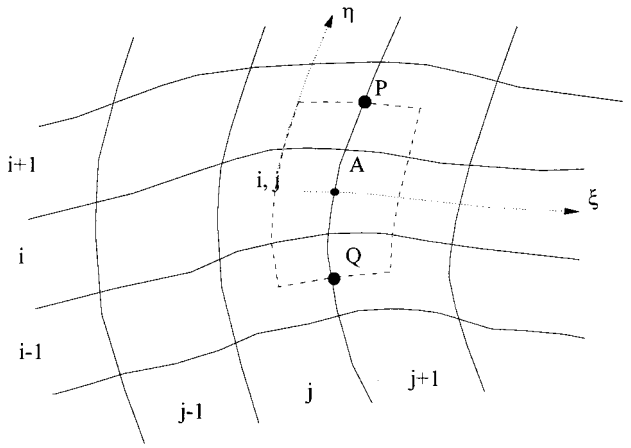

Figure 4. Evaluation of first-order derivatives.

$$\frac{\partial(\cdot)}{\partial x} = \frac{\Delta(\cdot)_\xi \, \Delta y_\eta - \Delta(\cdot)_\eta \, \Delta y_\xi}{\Delta x_\xi \, \Delta y_\eta - \Delta x_\eta \, \Delta y_\xi}, \tag{28}$$

$$\frac{\partial(\cdot)}{\partial y} = \frac{\Delta(\cdot)_\xi \, \Delta x_\eta - \Delta(\cdot)_\eta \, \Delta x_\xi}{\Delta y_\xi \, \Delta x_\eta - \Delta y_\eta \, \Delta x_\xi}, \tag{29}$$

where $(\cdot)$ denotes u or v. For the interface A illustrated in Figure 4, the differences of u, v, x and y can be obtained using an auxiliary control volume Ω_A, i.e. $\Delta(\cdot)_\xi = (\cdot)_{i,\,j+1} - (\cdot)_{i,\,j}$ and $\Delta(\cdot)_\eta = (\cdot)_P - (\cdot)_Q$, where $(\cdot)_P$ is interpolated from cell values of $(\cdot)_{i-1,\,j}$ and $(\cdot)_{i-1,\,j+1}$, and $(\cdot)_Q$ is interpolated from cell values of $(\cdot)_{i-1,\,j}$ and $(\cdot)_{i-1,\,j+1}$,. To achieve second-order spatial accuracy, the values of the six cells encompassed by Ω_A are used to provide the numerical flux at cell interface A. The Jacobian approximation relies on some degree of smoothness of the mesh. If the mesh is very distorted, the above method may introduce geometric errors requiring special treatment.

3.3. Operator splitting and stability conditions

In order to discretise the convective terms separately, we split the shallow water equations into two parts, namely Equations (11) and (12). To maintain second-order accuracy in time, a symmetric sequence of split operators is used, i.e.

$$\boldsymbol{U}^{n+1} = L^{\mathrm{S}} L^{\mathrm{I}} L^{\mathrm{I}} L^{\mathrm{S}} \boldsymbol{U}^n, \tag{30}$$

where L^{I} and L^{S} denote split operators for the inviscid terms and source terms respectively.

Obviously, in practice, the stability restriction which applies to the two split equations will be different. If the time step allowed by the source terms is smaller than that allowed by the inviscid convective terms, i.e. $\Delta t_{\mathrm{S}} < \Delta t_{\mathrm{I}}$, this would imply an unnecessarily small time step for the convective terms which may create excessive artificial dissipation. The alternative is to use a single step of the explicit convective solver and k steps of the explicit source-term solver, i.e. $L^{\mathrm{I}}(\Delta t_{\mathrm{I}})[L^{\mathrm{S}}(\Delta t)]^k$, where $k = \boldsymbol{int}(\Delta t_{\mathrm{I}}/\Delta t)$, $\Delta t < \Delta t_{\mathrm{S}}$. When $\Delta t_{\mathrm{S}} \ll \Delta t_{\mathrm{I}}$, it is a *stiff* problem, and an implicit scheme for the source terms is required.

The following stability condition allows for the time step for the source terms being larger than the time step for the inviscid terms, namely $\Delta t_{\mathrm{S}} > \Delta t_{\mathrm{I}}$ [18]:

$$\frac{\sqrt{g}|u|}{C^2\sqrt{D}} < \frac{D}{\Delta\xi} < \frac{C}{6.26C_e}, \tag{31}$$

where C is the Chezy coefficient and D is the water depth. C_e is the turbulence eddy coefficient adjustable in the range of 0.1–1.0. $\Delta\xi$ is the length of a cell and u is the depth-averaged velocity. For most applications in coastal and river engineering, condition (31) is appropriate.

The scheme proposed here is an explicit scheme which is restricted by a CFL-like condition on the time step. For finite volume modelling, the following time step formulae are appropriate.

(i) Time step for 2D inviscid flows:

$$\Delta t_I = \alpha \min\left\{\frac{\Omega_{i,j}}{(\boldsymbol{q}_i \cdot \boldsymbol{S} + \beta c|\boldsymbol{S}_i| + \boldsymbol{q}_j \cdot \boldsymbol{S} + \beta c|\boldsymbol{S}_j|)}\right\}, \tag{32}$$

where Ω_{ij} is the cell area. The Courant number α is normally set to unity.

(ii) Time step for 2D source terms:

$$\Delta t_S = \min\left\{\frac{1}{(2\mu_{i,j}|\boldsymbol{S}_i|/\rho\Omega_{i,j}^2) + (2\mu_{i,j}|\boldsymbol{S}_j|/\rho\Omega_{i,j}^2) + (2g|u|/C^2D)}\right\}, \tag{33}$$

where μ_{ij} is the 'depth-averaged' turbulence eddy viscosity, and ρ is the fluid density.

3.4. Boundary conditions

Solid and *transmissive* boundary conditions are imposed as follows,

(i) Solid boundaries

A fixed reflective solid boundary is given by

$$\phi_{M+1} = \phi_M, \qquad u_{M+1} = -u_M, \qquad v_{M+1} = -v_M$$

$$\phi_{M+2} = \phi_{M-1}, \qquad u_{M+2} = -u_{M-1}, \qquad v_{M+2} = -v_{M-1},$$

where $M-1$ and M denote the last two cells inside the computational domain (Figure 5). $M+1$ and $M+2$ are two fictitious cells ('ghost cells') outside the computational domain.

(ii) Transmissive boundaries

Transmissive boundaries, also called 'transparent boundaries', allow waves to pass through without reflection. The transmissive boundaries are obtained by imposition of

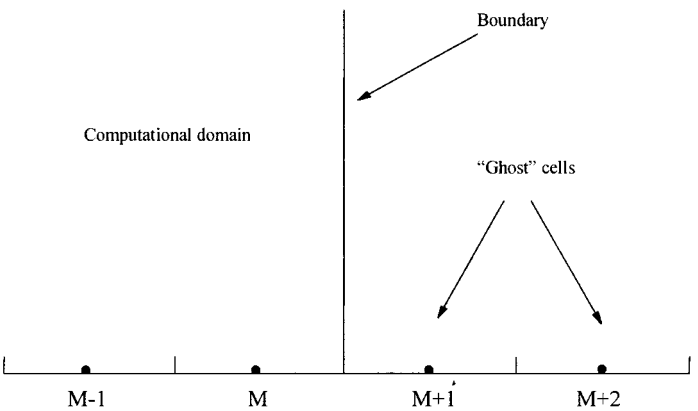

Figure 5. Sketch of computational cells inside and outside boundary.

$$\phi_{M+1} = \phi_M, \qquad u_{M+1} = u_M, \qquad v_{M+1} = v_M,$$

$$\phi_{M+2} = \phi_{M-1}, \qquad u_{M+2} = u_{M-1}, \qquad v_{M+2} = v_{M-1}.$$

We found this transmissive boundary treatment works very well in 1D and 2D hydraulic flow modelling.

The above two boundary conditions maintain second-order accuracy.

4. TEST PROBLEMS

Four test problems are considered to assess the schemes presented in Section 3. The van Leer slope limiter is adopted for all tests. The time step is limited by formulae (32) and (33). The Courant number α is set to unity.

4.1. Test 1: 1D dam break

In this case, we consider a straight channel, with the headwater and tailwater separated by a dam. The channel is flat-bottomed, and bed friction is ignored. The turbulence effects of currents are not considered. The momentum correction factor β is set to unity. Initially, the water has a different depth on each side of the dam, D_L and D_R (Figure 6) and the water is assumed to be at rest. At time $t = 0$, the dam is instantly and totally removed. It creates a *bore* wave moving from left to right, and a *depression* wave, or *rarefaction* wave, propagating towards the left.

The 1D dam break is a very useful bench-mark test with a known exact solution. It provides extreme conditions to assess the numerical stability of the model and illustrate the effects of artificial viscosity introduced by the scheme.

In this test, the length of a fixed region is set to 1.0 m with a barrier at $x = 0.5$ m.

4.2. Test 2: oblique hydraulic jump

The geometry is a 40-m long flat-bottomed channel where the upstream entry width of 30 m is narrowed to 28.43 m at the exit by a converging wall deflected through an angle $\theta = 8.96°$ (Figure 7). The chosen initial conditions were water depth $D_0 = 1$ m, $u_0 = 8.57$ m s^{-1} and

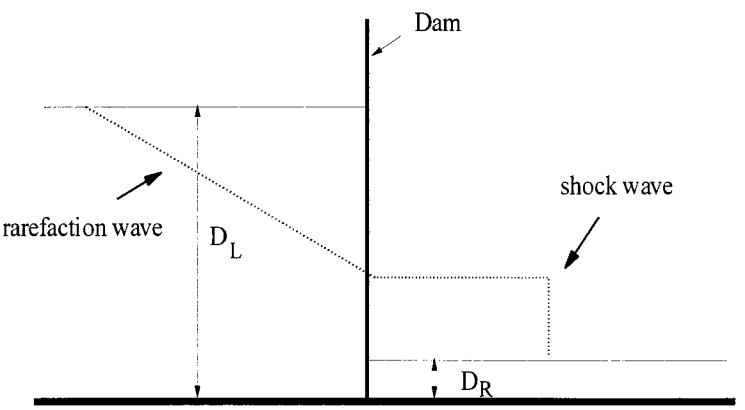

Figure 6. Test 1: dam break problem.

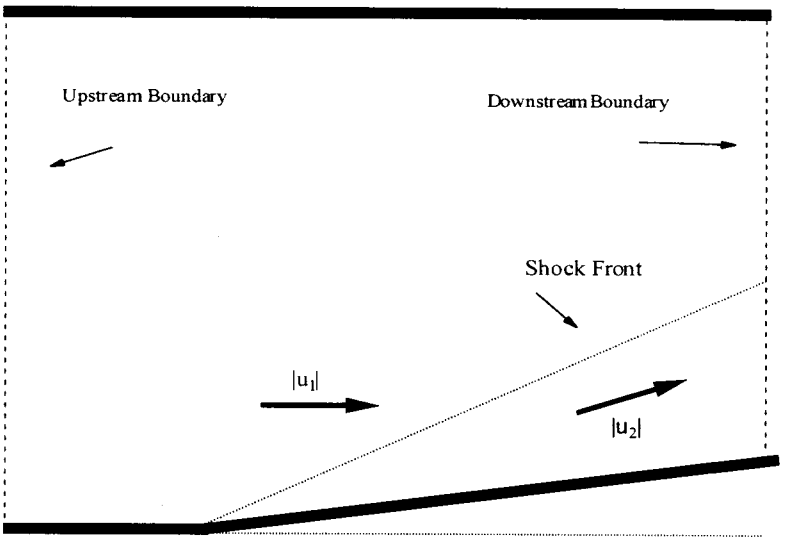

Figure 7. Test 2: sketch of oblique hydraulic jump.

$v_0 = 0$ m s^{-1}. Supercritical boundary conditions of $D = 1$ m, $u = 8.57$ m s^{-1} and $v = 0$ m s^{-1} ($Fr = 2.736$) were imposed at the upstream boundary. Transmissive boundary conditions were imposed at the downstream boundary. Friction along the channel walls is ignored. The momentum correction factor β was set to unity. The test case is a steady inviscid flow calculation. In this model, non-rectangular mesh was used (Figure 8).

This is a very useful standard test for 2D hydraulic flow modelling because the characteristics of the induced oblique shock front can be derived by theoretical analysis [21].

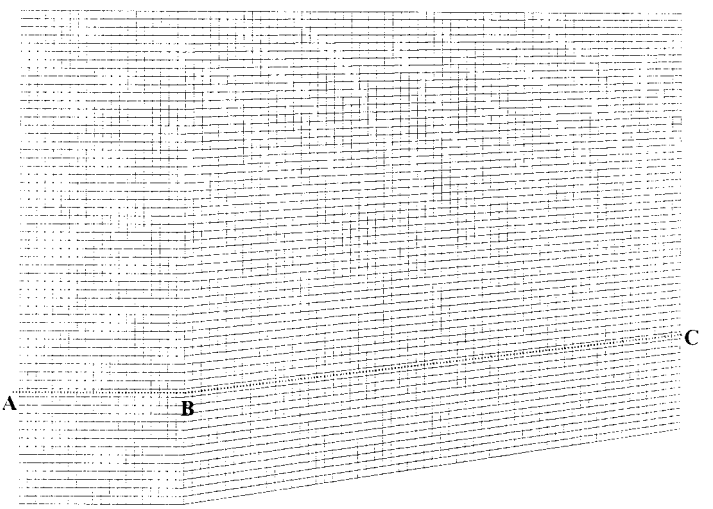

Figure 8. Test 2: computational grid (60×80) for oblique hydraulic jump.

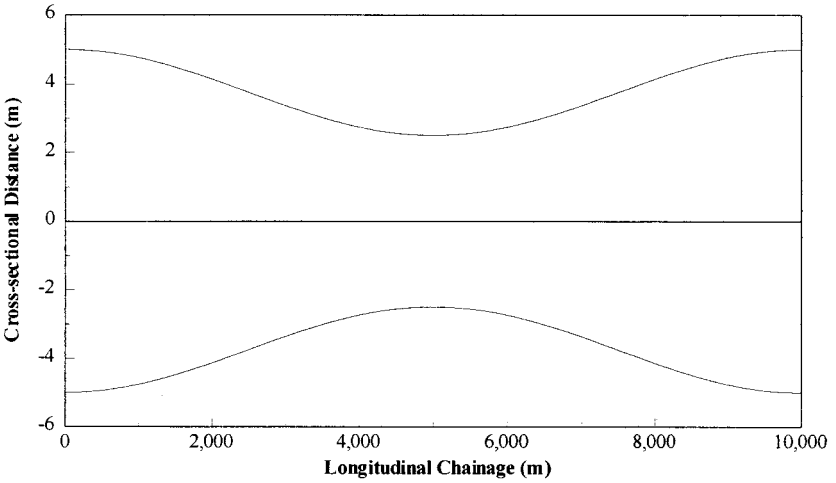

Figure 9. Test 3: sketch of a channel with varying width.

4.3. Test 3: flow in a channel with varying width and bed slope

The geometry is a channel 10 000 m long, in which the width varies from 5 to 10 m (see Figure 9). The bed slope is taken to be a constant value (1:100 and 1:50), except between $x = 4500$ and 5500 m where twice this value is taken (Figure 10). At the upstream boundary, a discharge $Q = 20$ m^3 s^{-1} is specified, i.e. $(\phi v)_{\text{upstream}} = Q^* g/b$, where g is the gravitational acceleration and b is the channel width. ϕ_{upstream} is extrapolated from the interior. A transmissive boundary condition was applied at the downstream boundary. The Manning formula was used for the bed friction and coefficient 'n' was set to 0.03. This test problem was used by Priestley [22] and Glaister [1].

In our modelling, a boundary-fitted 1D mesh was used (Figure 11). This demonstrates that a finite volume model based on the shallow water equations can be used directly for 1D river flow modelling.

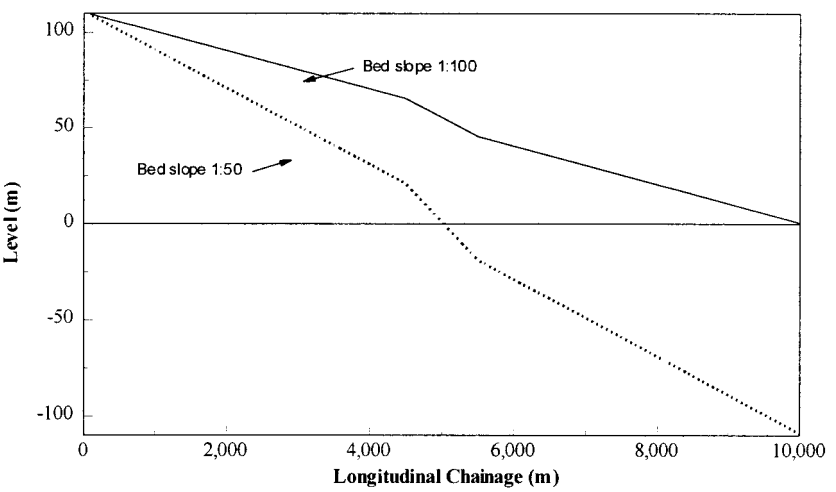

Figure 10. Test 3: sketch of a channel with varying slope.

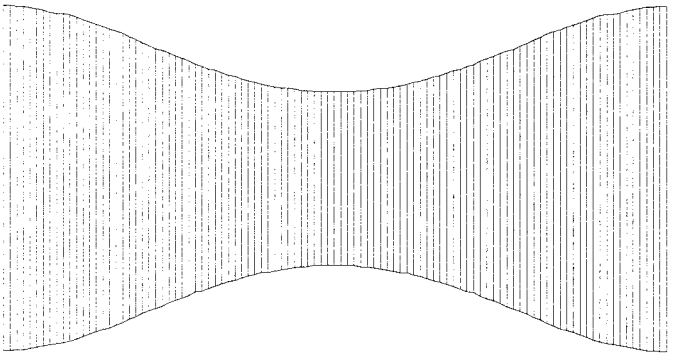

Figure 11. Test 3: computational grid ($\Delta\xi = 100$ m) for flow in a channel with varying width and bed slope.

4.4. Test 4: tidal bore wave

The tidal bore, a moving hydraulic jump, is a marvellous natural phenomenon which occurs in only a few river estuaries in the world. Because the tidal bore is born initially in a region at subcritical flow conditions, it provides a unique opportunity to test the model not only for numerical stability but also the ability to capture shock waves. Numerical modelling to simulate the formation and propagation of a tidal bore in a river estuary is rarely reported.

Although this is an imaginary river channel, its dimensions and bed slope are taken from the lower reaches of the River Severn, Gloucester, UK [23]. A 100-km length of the river is covered. The river is 10 km wide at the entrance. The width decreases linearly to just 100 m at the end. The river is tidal influenced with a tidal range of 9 m and period of 12.4 h. The channel ends with a weir with crest level of 6 m above datum. The bed slope is 1:10 000. The bed level at the river mouth is 10 m below the datum. The toe level of the weir is 0.0 m above the datum. The fresh water discharge from upstream of the weir is 5 $m^3\ s^{-1}$. It is assumed that no lateral inflows join the river.

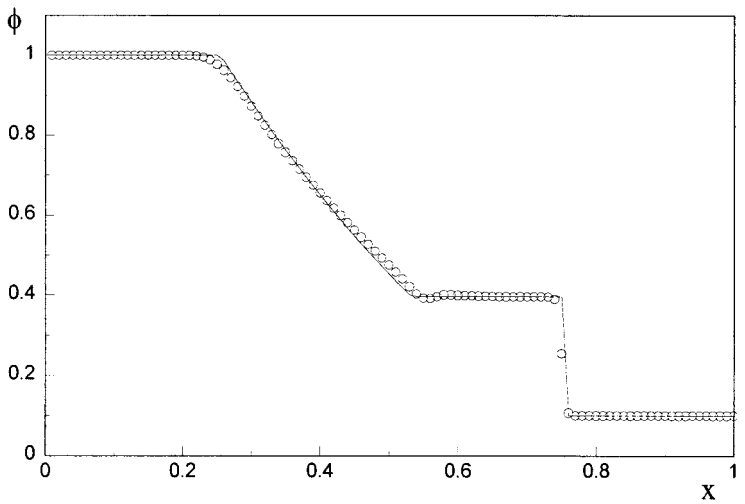

Figure 12. Test 1: water elevation after dam break with initial water depth ratio $\phi_L/\phi_R = 10{:}1$ ($t = 0.25$ s).

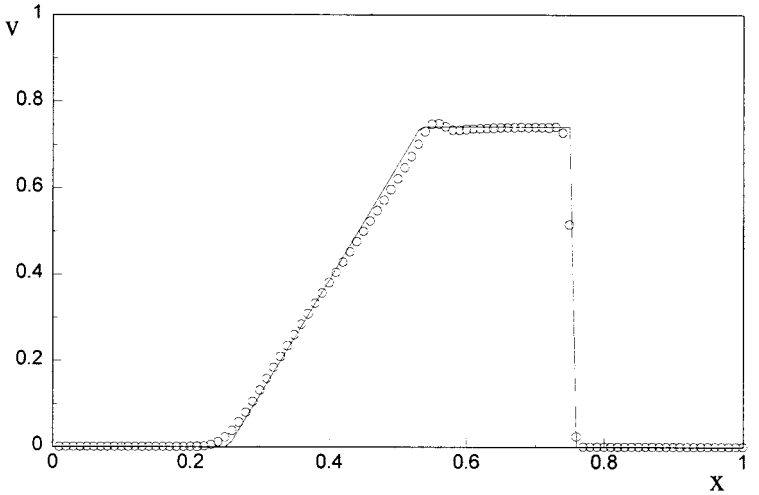

Figure 13. Test 1: water velocity after dam break with initial water depth ratio $\phi_L/\phi_R = 10{:}1$ ($t = 0.25$ s).

To simulate the interesting phenomenon of shoaling of tidal waves, a steeper bed slope of 1:3000 is also included. The set-up of the model is the same as the one described above, except the bed level at the river mouth is 30 m below the datum and the toe level of the weir is 3.33 m above the datum. The shoaling of tidal waves could be important in the design of river flood defences.

A sinusoidal time-series tidal curve of water depth is applied at the river mouth. At the upstream boundary, a fixed water level of 6 m above the datum is used when the water level at the end of the channel is lower than the crest level of the weir; the 'transmissive' boundary condition is applied when the water level is above the crest level. Similar to Test 3, a boundary-fitted 1D mesh is used.

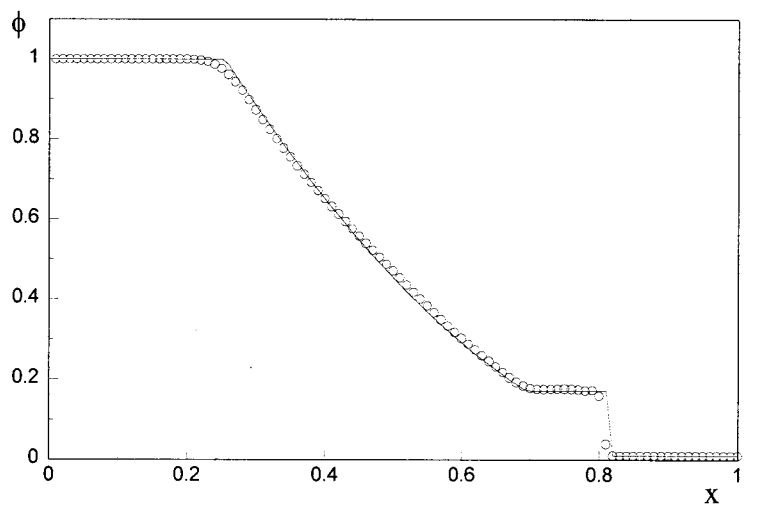

Figure 14. Test 1: water elevation after dam break with initial water depth ratio $\phi_L/\phi_R = 100{:}1$ ($t = 0.25$ s).

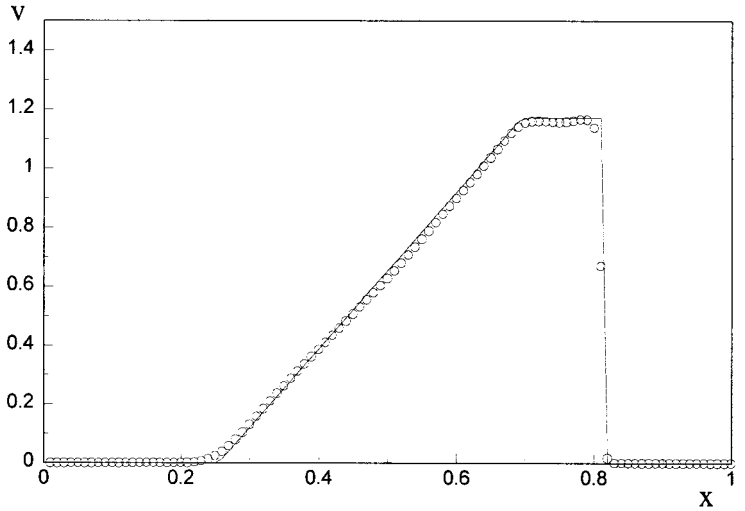

Figure 15. Test 1: water velocity after dam break with initial water depth ratio $\phi_L/\phi_R = 100{:}1$ ($t = 0.25$ s).

5. NUMERICAL RESULTS

5.1. Test 1: 1D dam break

Figures 12–15 present the results for the 1D dam break with $\phi_L/\phi_R = 10$ and 100. In the modelling, 100 computational cells are used, i.e. the spatial step $\Delta\xi$ is set to 0.1 m. The numerical results compare very well with the exact solutions, and show that the scheme is stable and that little spurious artificial viscosity is introduced. In particular, the right travelling bore is accurately resolved over only three cells and its height is given almost perfectly.

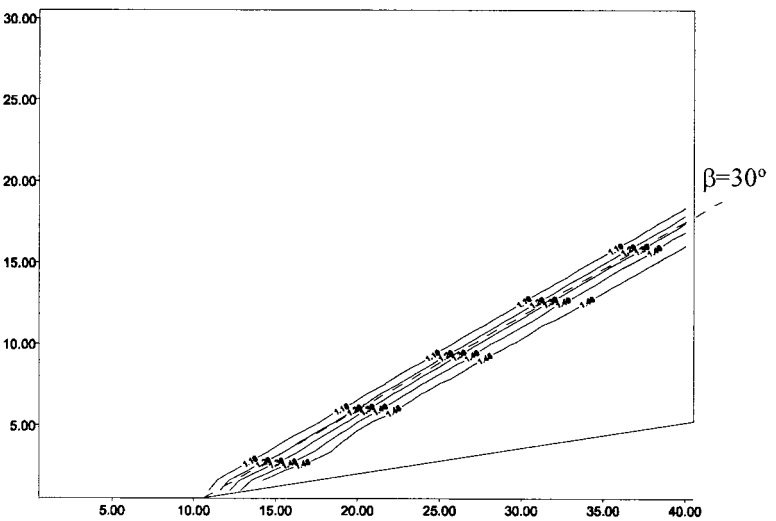

Figure 16. Test 2: depth contours showing the oblique shock front (mesh size 60×80).

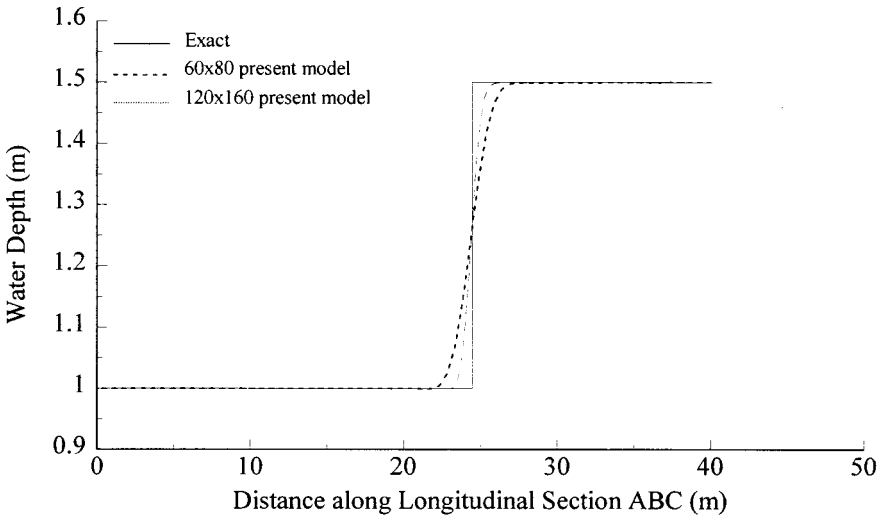

Figure 17. Test 2: water depth along the longitudinal section line ('ABC' shown in Figure 8).

5.2. Test 2: oblique hydraulic jump

A steady state solution is assumed to have been reached when the following convergence condition is satisfied:

$$\left(\frac{\phi^{n+1}-\phi^{n}}{\phi^{n}}\right)_{\max} \leq 10^{-6}.$$

Two computational meshes of 60×80 cells and 120×160 cells are used in the test. The results are presented as depth contour (Figure 16) and longitudinal sectional plots (Figure 17). The oblique hydraulic jump is well captured and clearly shown in the plots.

If the mesh is aligned at the known bore angle, the method resolves the standing bore exactly. This is to be expected since a finite volume method based on conservative variables implicitly invokes the correct bore jump relations when the mesh is aligned at the bore angle. The cases computed illustrate that this method is still able to resolve the bore accurately even when the mesh is non-aligned.

Good agreement between theoretical analysis and the numerical results is shown in Table I.

Table I. Comparison of results from the theoretical analysis and numerical model

	The angle of the shock front (β)	Velocity at the right side of shock ($\lvert u_2 \rvert$)	Water depth at the right side of shock (D_2)
		(m s^{-1})	(m)
Exact solutions	$\approx 30°$	7.956	1.5
Numerical solutions (60×80 mesh)	$\approx 30°$	7.954	1.499
Numerical solutions (120×160 mesh)	$\approx 30°$	7.957	1.500

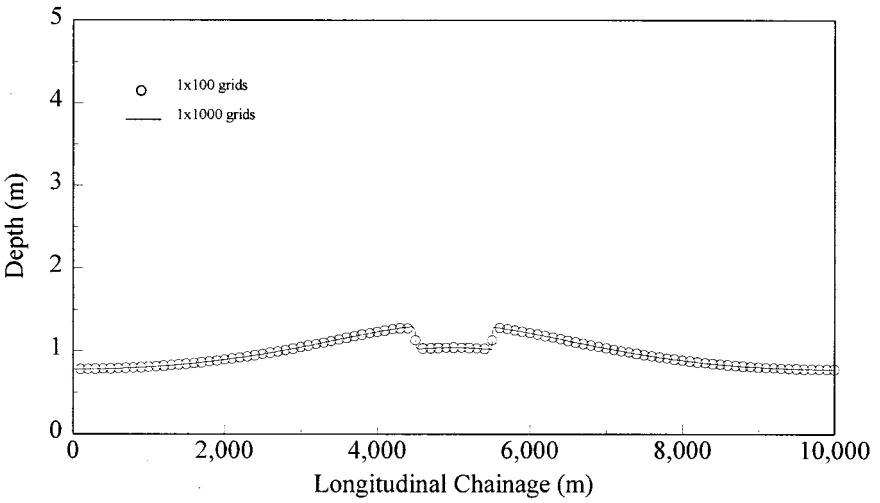

Figure 18. Test 3: depth for a bed slope of 1:100.

5.3. Test 3: flow in a channel with varying width and bed-slope

Two computational meshes with spatial steps of $\Delta\xi = 100$ and 10 m are used in this test. The results are shown in Figures 18–21. Compared with a bed slope of 1:50, which gives supercritical flow everywhere, it is noted that supercritical flow only exists locally between the chainage 4500 and 5500 m for the bed slope of 1:100. The stationary bores induced by the sudden change of bed slope are well captured. In the Froude number plots there are no obvious numerical oscillations around shock fronts, which were observed in the results produced by Glaister [1]. The fact that the results from the coarse mesh agree well with the results from the fine mesh shows the high-resolution property of the scheme. The results appear to show improvement over those of other schemes such as Priestley's (given by Glaister [1]).

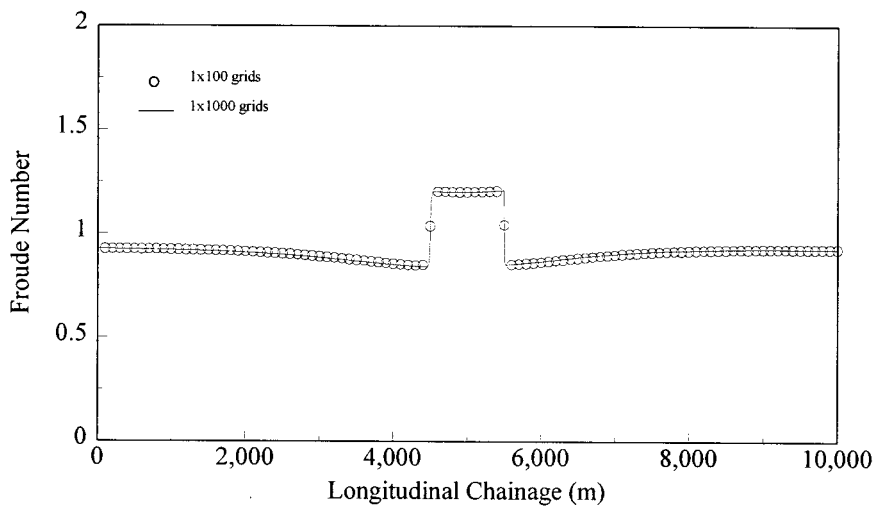

Figure 19. Test 3: Froude number for a bed slope of 1:100.

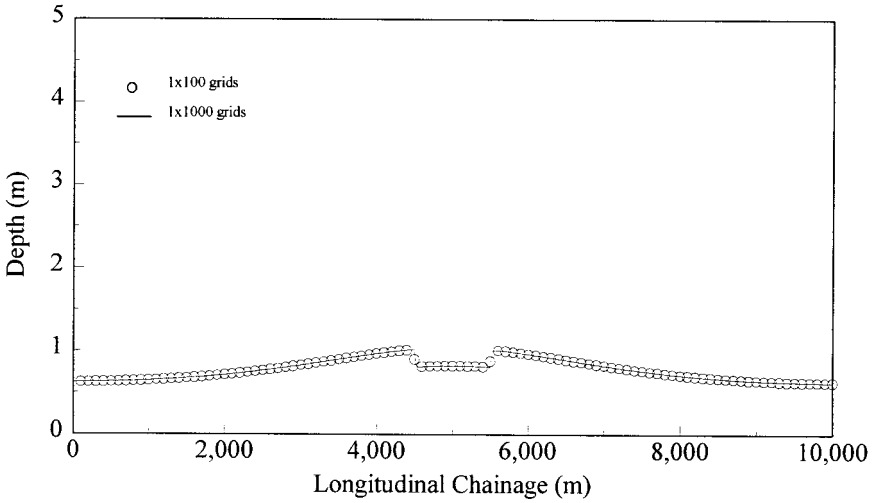

Figure 20. Test 3: depth for a bed slope of 1:50.

5.4. Test 4: tidal bore wave

The results are illustrated in Figures 22 and 23. In the modelling, a spatial step of $\Delta\xi = 50$ m is used. The formation of the tidal bores is clearly represented. The results show that the bores travels at speeds of 16.9 and 9.1 km h^{-1} for the bed slope of 1:10 000 and 1:3000 respectively. The phenomenon of the shoaling of tidal waves is shown in the results of the test with a steep bed slope (Figure 23). Although there is no measured or experimented data to prove its accuracy, the results are very encouraging.

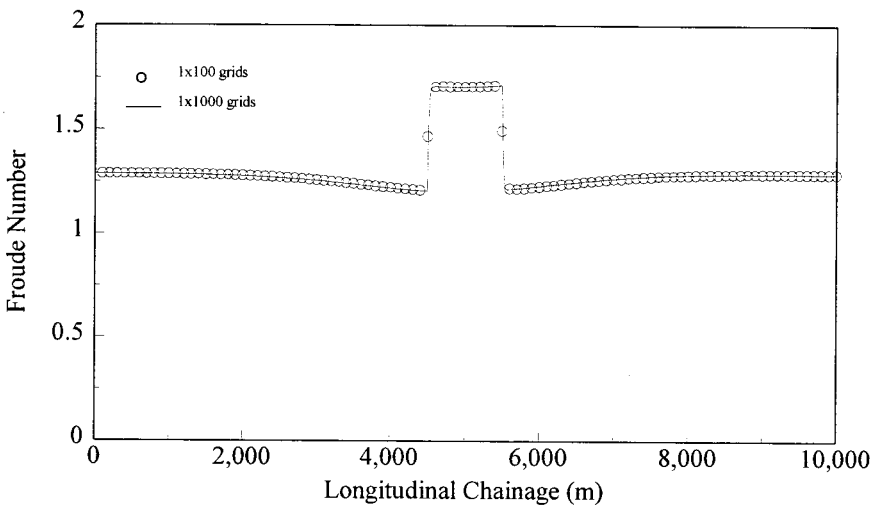

Figure 21. Test 3: Froude number for a bed slope of 1:50.

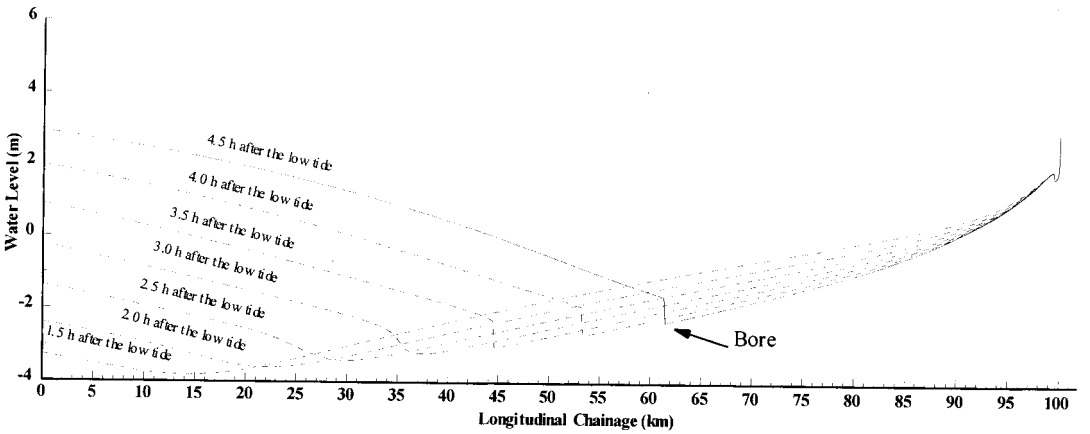

Figure 22. Test 4: Simulation of formation and propagation of tidal bore (bed slope 1:10 000).

6. CONCLUSIONS

A high-resolution finite volume model is presented for hydraulic flows. Second-order accuracy has been achieved by means of MUSCL reconstruction in conjunction with a Hancock two-stage scheme for the time integration. A HLL approximate Riemann solver has been used. The TVD property of the scheme is ensured by applying a pre-processing slope limiter. The scheme is robust and capable of simulating transcritical flows and capturing hydraulic jumps. The new scheme introduces little spurious artificial viscosity and has excellent numerical stability. The scheme has been validated against standard test problems for which there exist exact solutions and has been applied to idealised problems of interest. The method is useful for modelling 1D or 2D river flows, particularly in cases where transcritical flows and hydraulic jumps occur.

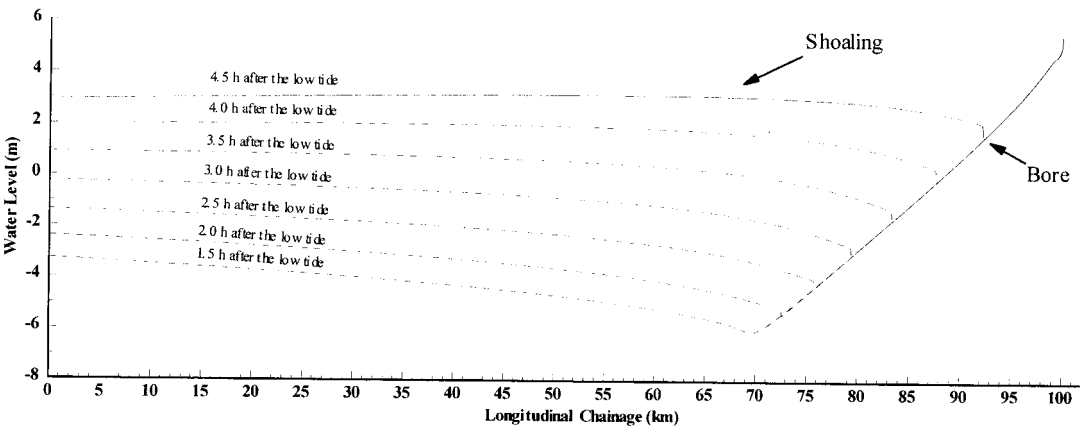

Figure 23. Test 4: Simulation of formation and propagation of tidal bore (bed slope 1:3000).

REFERENCES

1. P. Glaister, 'Flux difference splitting for open-channel flows', *Int. J. Numer. Methods Fluids*, **16**, 629–654 (1993).
2. P.D. Lax and B. Wendroff, 'Systems of conservation laws', *Comm. Pure Appl. Math.*, **13**, 217–237 (1960).
3. S.K. Godunov, 'A difference method for the numerical calculation of discontinuous solutions of hydrodynamic equations', *Matemsticheskly Sboraik*, **47**, 1959 (US Joint Publications Research Service).
4. A. Harten, P.D. Lax and B. van Leer, 'On upstream differencing and Godunov-type schemes for hyperbolic conservation laws', *SIAM Rev.*, **25**, 35–61 (1983).
5. P.L. Roe, 'Approximate Riemann solvers, parameter vectors and difference schemes', *J. Comput. Phys.*, **43**, 357–372 (1981).
6. S. Osher, 'Numerical solution of singular perturbation problems and hyperbolic systems of conservation laws', in O. Axelsson *et al.* (eds), *Mathematical Studies*, Vol. 47, North Holland: Amsterdam, 1981.
7. R. Rajar, 'Mathematical simulation of dam-break flow', *J. Hydraul. Div., ASCE*, **104**, 1011–1026 (1978).
8. R. Garcia, 'Numerical solution of the St. Venant equations with the MacCormack finite-difference scheme', *Int. J. Numer. Methods Fluids*, **6**, 259–274 (1986).
9. R.J. Fennema and M.H. Chaudhry, 'Explicit methods for 2-D transient free-surface flows', *J. Hydraul. Eng.*, **116**, 1013–1034 (1990).
10. F. Alcrudo and P. Garcia-Navarro, 'A high-resolution Godunov-type scheme in finite volumes for the 2D shallow-water equations', *Int. J. Numer. Methods Fluids*, **16**, 489–505 (1993).
11. P. Glaister, 'Approximate Riemann solutions of the shallow water equations', *J. Hydraul. Res.*, **26**, 293–306 (1988).
12. E.F. Toro, 'Riemann problems and the WAF method for solving the two-dimensional shallow water equations', *Phil. Trans. R. Soc. Lond., A*, **338**, 43–68 (1992).
13. J.Y. Yang and C.A. Hsu, 'Computations of free surface flows part 2: two-dimensional unsteady bore diffraction', *J. Hydraul. Res.*, **31**, 403–414 (1993).
14. B.H. Johnson and J.F. Thompson, 'A discussion of boundary-fitted coordinate systems and their applicability to the numerical modelling of hydraulic problem', *Misc. Paper HL-78-9*, Mississippi State University, 1978.
15. F. Alcrudo and P. Garcia-Navarro, 'A high-resolution Godunov-type scheme in finite volumes for the 2D shallow-water equations', *Int. J. Numer. Methods Fluids*, **16**, 489–505 (1993).
16. R.A. Falconer, 'Mathematical modelling of jet-forced circulation in reservoirs and harbours', *Ph.D. Thesis*, Imperial College, London, 1976.
17. G. Strang, 'On the construction and comparison of difference schemes', *SIAM J. Numer. Anal.*, **5**, 506–517 (1968).
18. K. Hu, 'High-resolution finite volume methods for hydraulic flow modelling', Internal Report, *The Manchester Metropolitan University*, England, 1996.
19. G.D. van Albada, B. van Leer and W.W. Roberts, Jr., 'A comparative study of computational methods in cosmic gas dynamics', *Astron. Astrophys.*, **108**, 76–84 (1982).
20. G.S. Deiwert, 'Numerical simulation of high Reynolds number transonic flows', *AIAA J.*, **13**, 1354–1359 (1975).
21. F.M. Henderson, *Open Channel Flow*, Macmillan: New York, 1966.
22. A. Priestley, 'A quasi-Riemann method for supercritical, open-channel flow', *Numerical Analysis Report*, University of Reading, 1991.
23. F.W. Rowbotham, *The Severn Bore*, David & Charles, Devon, 1983.

